Yi *et al. Chem Synth* 2024;4:67
DOI: 10.20517/cs.2024.60

Chemical Synthesis

Research Article

Open Access

Check for updates

Co single atoms/nanoparticles over carbon nanotubes for synergistic oxidation of 5-hydroxymethylfurfural to 2,5-furandicarboxylic acid

Chengfeng Yi, Zhigang Liu*

Advanced Catalytic Engineering Research Center of the Ministry of Education, College of Chemistry and Chemical Engineering, Hunan University, Changsha 410082, Hunan, China.

***Correspondence to:** Prof. Zhigang Liu, College of Chemistry and Chemical Engineering, Hunan University, Lushan South Road No.2, Changsha 410082, Hunan, China. E-mail: liuzhigang@hnu.edu.cn

How to cite this article: Yi C, Liu Z. Co single atoms/nanoparticles over carbon nanotubes for synergistic oxidation of 5-hydroxymethylfurfural to 2,5-furandicarboxylic acid. *Chem Synth* 2024;4:67. https://dx.doi.org/10.20517/cs.2024.60

Received: 15 May 2024 **First Decision:** 18 Jul 2024 **Revised:** 20 Aug 2024 **Accepted:** 6 Sep 2024 **Published:** 5 Nov 2024

Academic Editors: Ying Wan, Yuefeng Liu **Copy Editor:** Dong-Li Li **Production Editor:** Dong-Li Li

Abstract

The preparation of high-value 2,5-furandicarboxylic acid (FDCA) from biomass-based platform compound 5-hydroxymethylfurfural (HMF) is an important synthetic reaction, as the resulting FDCA holds promise to replace terephthalic acid to produce environmentally friendly polyester materials. However, due to the complex tandem nature of the oxidation of HMF to FDCA, which involves several stable intermediates, efficient conversion of HMF and achieving a high FDCA yield remain challenging. Herein, a catalyst of Co SAs/NPs@N-CNTs comprising Co single atoms (Co SAs) alongside Co nanoparticles (Co NPs) supported on carbon nanotubes (CNTs) was synthesized. Co SAs/NPs@N-CNTs exhibited outstanding catalytic activity for the selective oxidation of HMF to FDCA, achieving 100% HMF conversion and 94.2% FDCA yield. This remarkable performance was attributed to the synergistic effect between Co SAs and Co NPs. Poisoning and acid treatment experiments indicated that Co SAs served as the active sites, while Co NPs did not directly act as active sites. Instead, Co NPs merely assisted the Co SAs on the sidelines, facilitating the efficient conversion of HMF into various intermediates and promoting the further conversion of these intermediates into FDCA, thereby achieving high FDCA productivity. This strategy offers new insights for designing efficient catalysts for complex tandem reactions.

Keywords: Oxidation of 5-hydroxymethylfurfural, 2,5-furandicarboxylic acid, Co single atoms, Co nanoparticles, synergistic effect

INTRODUCTION

As the social economy advances, the resource problem is pressing. It is urgent and necessary to reduce reliance on fossil fuels and explore renewable green sources, such as biomass resources. One of the biomass sources, lignocellulose, can be obtained from wood, waste paper, agricultural residues (e.g., corn stover), and municipal solid waste. Biomass-based platform compounds derived from lignocellulose can be further fermented to produce ethanol fuel or chemically converted into high-value chemicals[1]. 5-hydroxymethylfurfural (HMF) is a key biomass-derived platform compound, featuring both hydroxyl and aldehyde groups connected to the furan ring. It can undergo a series of chemical reactions to convert into highly valuable derivatives[2,3]. The product of HMF oxidation, 2,5-furandicarboxylic acid (FDCA), shares structural and chemical similarities with terephthalic acid. Furthermore, FDCA exhibits biodegradability and environmental friendliness, making it superior to terephthalic acid. Apart from being bio-based and biodegradable, polyesters synthesized from FDCA have the potential to be recycled to their monomers using existing de-polymerization technologies[4,5]. According to relevant statistics, if FDCA is used as the raw material to produce polyester materials instead of terephthalic acid, the global consumption of non-renewable resources can be greatly reduced, and greenhouse gas emissions can also be significantly decreased[6,7].Therefore, efficiently synthesizing FDCA and potentially replacing terephthalic acid with FDCA in the synthesis of polyester materials is widely regarded as a very meaningful endeavor.

In recent years, researchers have developed various catalysts for the synthesis of FDCA from HMF[8,9]. Typical catalysts include noble metal catalysts such as Pd, Pt, Au and Ru[10-13]. Noble metal catalysts typically exhibit high conversion and selectivity in the oxidation of HMF to FDCA. Nevertheless, the broad industrial application of noble metal catalysts is constrained by the limited availability and high cost. Consequently, there has been a rise in the development of non-noble metal catalysts. Yang *et al.* prepared nitrogen-doped graphene-encapsulated Cu nanoparticles[14]. After 16 h of reaction time, the FDCA yield reached 58%. Zhang *et al.* prepared a series of bimetallic oxides (Mn-Co-O) through hydrothermal process[15]. Under molecular oxygen and weak alkaline conditions, $MnCo_2O_4$ with hollow hexagonal structure exhibited the highest FDCA yield, reaching 70.9% after reacting at 100 °C for 24 h. Even with certain catalytic activity, these catalysts still have limitations in terms of conversion and selectivity, making it challenging to efficiently obtain the final product FDCA.

The selective oxidation of HMF to FDCA involves a complex tandem reaction: HMF needs to be first oxidized to 2,5-diformylfuran (DFF) or 5-hydroxymethyl-2-furancarboxylic acid (HMFCA), and then DFF or HMFCA is further oxidized to 5-formyl-2-furancarboxylic acid (FFCA), which finally converts to FDCA[16]. All three intermediates (DFF, HMFCA, FFCA) can exist stably. To ensure a high yield towards the desired final product FDCA, it is essential to facilitate the complete conversion of HMF into intermediates and to promote the subsequent transformation of these intermediates towards FDCA. Most catalysts struggle with efficiently converting each intermediate at individual active sites, leading to an overall low efficiency in obtaining FDCA. Some studies have shown that composite systems of nanoparticles or clusters and single atoms can effectively promote multi-step reaction[17-19]. For example, Yi *et al.* loaded an appropriate amount of cobalt porphyrin onto hollow carbon spheres, obtaining a composite catalyst with Co single atoms (Co SAs) and CoO clusters coexisting[18]. This catalyst demonstrated exceptional catalytic performance in the multi-step reaction of ethylbenzene oxidation to acetophenone. The acetophenone yield reached 96% after 12 h of reaction time. This is because the coexisting CoO clusters synergistically promoted the breaking of the α-C-H bond of ethylbenzene on the active sites of Co SAs, which happened to be the rate-determining step. Tan *et al.* prepared N-doped carbon nanomaterials with CoO_X clusters and Co SAs coexisting using metal-organic framework (MOF) confinement strategy[19]. The Co-N_X single atom sites effectively adjusted the charge distribution of CoO_X clusters, downshifting the d-band center of Co

adsorption sites in CoO_X clusters. As a result, the reaction barriers for O_2* and OH* and the overpotential of OER were lowered, accelerating the overall OER kinetics. Consequently, it is feasible to design a catalyst containing both nanoparticles or clusters and single atoms for efficient oxidation of HMF to FDCA.

Herein, a catalyst with Co SAs and Co nanoparticles (Co NPs) coexisting was designed to overcome the issue of insufficient kinetics for complex tandem reactions occurring at individual active sites. The catalyst was prepared by impregnating carbon nanotubes (CNTs) with 5,10,15,20-tetraphenyl porphin (TPP) and metal cobalt salts, followed by further calcination. During the impregnation process, TPP coordinated with Co^{2+} to form Co-N_X structures, which facilitated the formation of single atoms and effectively suppressed the excessive aggregation of Co species during subsequent calcination. The presence of Co SAs and Co NPs allows each to contribute uniquely to the effective conversion of HMF and its intermediates, ultimately leading to the effective formation of FDCA.

EXPERIMENTAL

Materials

Benzaldehyde (C_7H_6O), propionic acid ($C_3H_6O_2$), hydrochloric acid (HCl), pyrrole (C_5H_5N), dichloromethane (CH_2Cl_2), 200-300 mesh silica gel, cobalt chloride hexahydrate ($CoCl_2$ $6H_2O$) and dimethyl sulfoxide (DMSO) were obtained from Sinopharm Chemical Reagent Co., Ltd. HMF (99%), HMFCA (98%) and 2,6-di-tert-butyl-p-cresol (BHT) were obtained from Aladdin. FDCA (98%), FFCA (98%), DFF (98%) and tert-butyl hydroperoxide (TBHP) (70% in water) were obtained from Mackin Ltd. Above chemicals were used without further purification. CNTs were purchased from Chengdu Zhongke Times Nanotechnology Co., Ltd and subjected to acid treatment before use. The acid treatment of CNTs is described in Section "Synthesis of Co@CNTs".

Synthesis of TPP

The preparation of TPP is based on the literature previously reported by our group[20]. In a 500 mL of three-neck flask, precise amounts of benzaldehyde (7.3 g) and 220 mL of propionic acid as the solvent were combined and heated to reflux at 135 °C under magnetic stirring. Subsequently, 30 mL of propionic acid with 5 mL of freshly distilled pyrrole was gradually added to the above mixture, which was further refluxed for 1 h. Afterward, 100 mL of H_2O was added. After leaving the mixture in the refrigerator overnight, the mixture was filtered, and the residue was washed with H_2O and dried to yield the crude product. The crude product was then separated by column chromatography using 200-300 mesh silica gel as the adsorbent and CH_2Cl_2 as the eluent to collect the second fraction. After removing the eluent with rotary evaporation, the pure product, TPP, was obtained after drying at 80 °C.

Synthesis of Co@CNTs

Commercial CNTs were subjected to acid treatment, referring to previous studies[18]. Specifically, 0.10 g of CNTs were placed in a round-bottom flask containing 20 mL of 2 mol L^{-1} HCl solution. The mixture was stirred at 80 °C for 12 h. After filtering and washing by deionized water, the acid-treated CNTs were obtained. Subsequently, 0.05 g of the treated CNTs was added into a flask. Then, 3.5×10^{-3} g of $CoCl_2$ $6H_2O$ and 20 mL of CH_2Cl_2 were added. The mixture was stirred at 40 °C for 12 h. After the solvent was evaporated, the residue was dried, ground and heated to 600 °C, holding this temperature for 2 h under N_2 atmosphere. Once cooling to room temperature, Co@CNTs were obtained.

Synthesis of Co SAs/NPs@N-CNTs and Co SAs@N-CNTs

In a flask, 3.5×10^{-3} g of $CoCl_2$ $6H_2O$ and 9.2×10^{-3} g of TPP were combined with 20 mL of CH_2Cl_2 and stirred until dissolved. Then, 0.05 g of acid-treated CNTs was introduced and stirred for 12 h. After removing the solvent, the residue was dried, ground and subsequently heated to 600 °C, maintaining the

temperature for 2 h. The final product, Co SAs/NPs@N-CNTs, was obtained. Additionally, 0.10 g of Co SAs/NPs@N-CNTs was placed in a flask with 20 mL of 2 mol L^{-1} HCl solution. The mixture was stirred at 80 °C for 12 h. Co SAs@N-CNTs was obtained after filtration and washing by H_2O.

Catalytic performance test

A precise amount of 20 mg of catalyst was weighed and placed in a reaction tube. Then, 5 mL of DMSO and 1.68 mL of TBHP were added as a solvent and an oxidant, respectively. Next, 0.1 mmol of HMF (12.6 mg) was added into the above reaction tube. The mixture was stirred at 80 °C for 24 h. Afterward, the reaction solution was taken and filtered through an organic filtration head, and then was analyzed through high performance liquid chromatography (HPLC, Shimadzu-SPD-20A). The conversion and yield were calculated using Equations (1) and (2). In addition, characterization details are provided in the Supplementary Materials.

$$\text{conversion (\%)} = \frac{\text{moles of converted HMF}}{\text{moles of initial HMF}} \times 100\% \quad (1)$$

$$\text{yield (\%)} = \frac{\text{moles of formed product}}{\text{moles of initial HMF}} \times 100\% \quad (2)$$

RESULTS AND DISCUSSION

Characterization of Co@CNTs and Co SAs/NPs@N-CNTs

From Supplementary Figure 1, it can be observed that there is no significant change in the morphology of CNTs after impregnation with $CoCl_2$ $6H_2O$ and TPP. Transmission electron microscopy (TEM) was conducted to examine the specific size of CNTs and the existence form of various species. The size of CNTs was found to be 20-50 nm [Figure 1A-D and F-I], and the carbon in both Co@CNTs and Co SAs/NPs@N-CNTs existed in the form of graphitic carbon [Figure 1D and I]. Additionally, distinct metal nanoparticles were observed in both Co@CNTs and Co SAs/NPs@N-CNTs (marked with red circles); however, the number and size of nanoparticles varied, and Co SAs/NPs@N-CNTs possessed fewer and smaller metal nanoparticles. The detailed distribution of metal particle sizes can be found in Supplementary Figure 2. High resolution transmission electron microscope (HR-TEM) images [Figure 1D and I] indicated that metal nanoparticles in Co@CNTs were assigned to CoO and Co_3O_4, with clear overlap between Co and O elements in the elemental distribution mapping [Figure 1E]. In contrast, there was no overlap between Co and O elements in the elemental distribution mapping of Co SAs/NPs@N-CNTs [Figure 1J]. The HR-TEM images only revealed lattice structures associated with the (111) plane of Co NPs in Co SAs/NPs@N-CNTs. Furthermore, the elemental distribution mapping highlighted the effective integration of nitrogen into the carbon framework. Doped N would form complexes with Co, effectively inhibiting the aggregation and growth of Co NPs during high-temperature annealing[21,22]. This phenomenon is particularly evident in Co SAs/NPs@N-CNTs, where fewer and smaller metal nanoparticles were observed. Doped N also prevented the further oxidation of Co NPs into CoO and Co_3O_4. Interestingly, compared to Co@CNTs, Co SAs/NPs@N-CNTs exhibited the presence of Co species not only in the form of distinct Co NPs but also potentially as Co SA active sites, as evident from numerous dispersed bright yellow spots in the Co elemental distribution mapping.

The graphitization and defect levels of the samples were estimated via Raman spectra [Figure 2A]. Two characteristic peaks were observed at 1,350 and 1,590 cm^{-1}, attributed to the D and G bands, respectively. The ratio of the D band intensity to G band intensity (I_D/I_G) is typically employed to assess the level of defect in the material. Co SAs/NPs@N-CNTs exhibited the highest I_D/I_G value, indicating the successful N doping and an increase in material defect level[23,24]. The X-ray diffraction (XRD) spectra [Figure 2B] for all samples

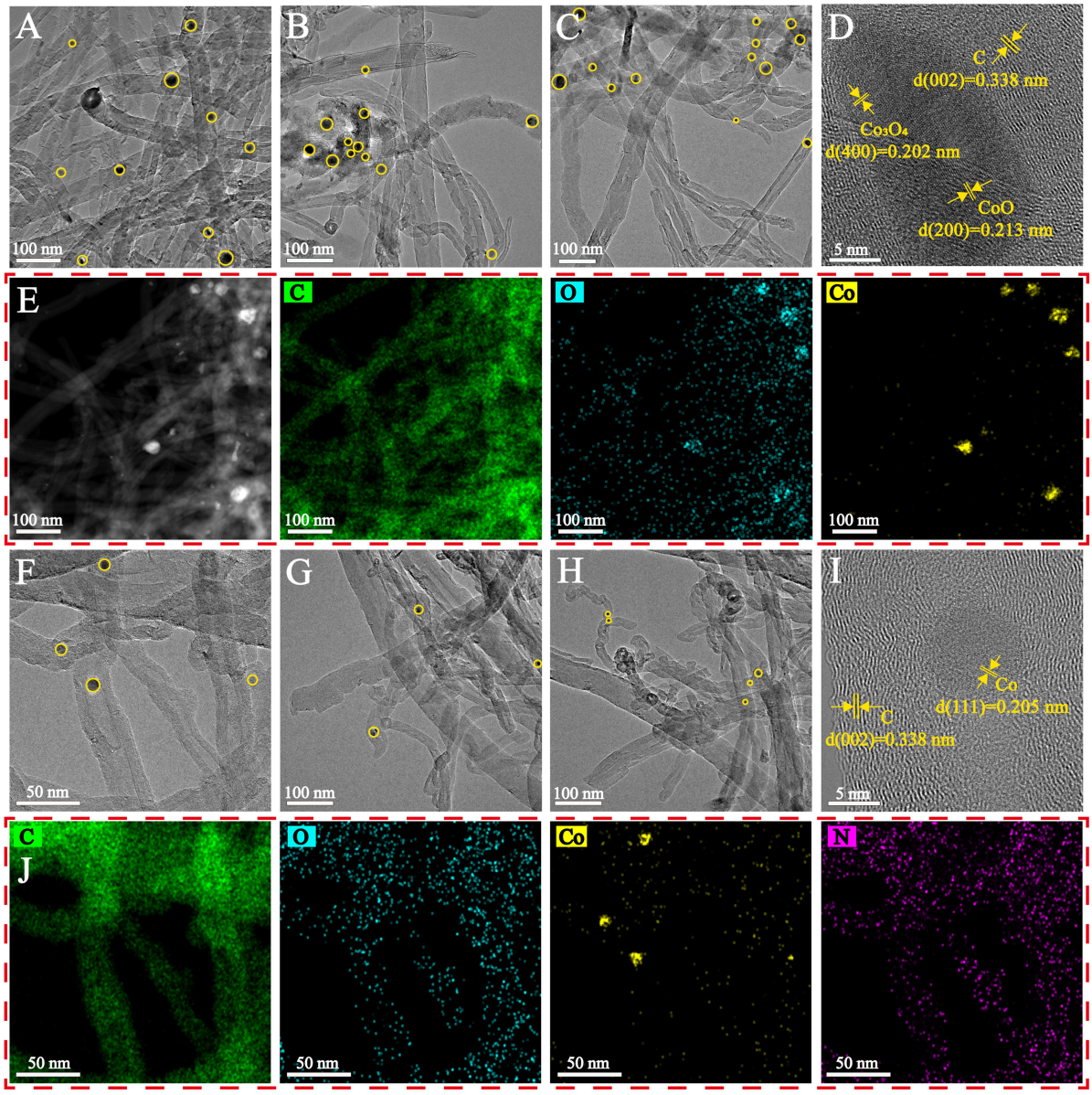

Figure 1. (A-C) TEM images of Co@CNTs under different vision; (D) HR-TEM image of Co@CNTs; (E) Element mapping of Co@CNTs for C, O, Co; (F-H) TEM images of Co SAs/NPs@N-CNTs under different vision; (I) HR-TEM image of Co SAs/NPs@N-CNTs; (J) Element mapping of Co SAs/NPs@N-CNTs for C, O, Co, N. TEM: Transmission electron microscopy; CNTs: carbon nanotubes; HR-TEM: high resolution transmission electron microscope; SAs: single atoms; NPs: nanoparticles.

exhibited diffraction peaks associated with the (002), (100), (101), and (004) planes of graphitic carbon. However, no distinct diffraction peaks were ascribed to Co or CoO_X nanoparticles, indicating that the Co species are either too small or too well-dispersed in Co@CNTs and Co SAs/NPs@N-CNTs to be detected by XRD. All catalysts presented the type-IV isotherm with an H3 hysteresis loop, suggesting that these catalysts were mesoporous material[25,26]. The introduction of $CoCl_2$ $6H_2O$ and TPP did not significantly affect the pore structure of CNTs [Supplementary Figure 3 and Supplementary Table 1], thereby preventing any impact of surface structure on their catalytic activity.

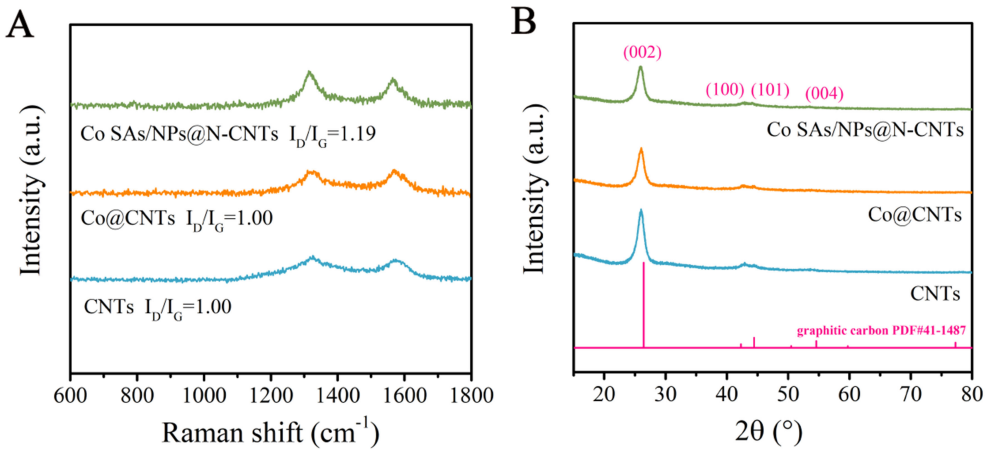

Figure 2. (A) Raman spectra and (B) XRD patterns of CNTs, Co@CNTs and Co SAs/NPs@N-CNTs. XRD: X-ray diffraction; CNTs: carbon nanotubes; SAs: single atoms; NPs: nanoparticles.

The X-ray photoelectron spectroscopy (XPS) full spectrum of Co SAs/NPs@N-CNTs [Figure 3A] showed an obvious peak of N 1s, and the C 1s spectrum of Co SAs/NPs@N-CNTs [Figure 3B] was deconvoluted into peaks at 284.8 eV (C-C), 285.5 eV (C=N), 286.2 eV (C-O), 287.3 eV (C=O) and 289.8 eV (π-π* conjugation)[27,28], indicating effective integration of nitrogen into the carbon framework. The doped N atoms were present as pyridinic N (398.9 eV), pyrrolic N (400.1 eV), graphitic N (401.2 eV), and oxidized N (403.2 eV)[20,29] [Figure 3C], with pyridinic N being the dominant form (constituting 48.0%) [Supplementary Table 2]; pyridinic nitrogen is known to readily create Co-N_X active sites[30,31]. The Co 2p spectrum of Co SAs/NPs@N-CNTs [Figure 3D] exhibited peaks attributed to Co^0 (780.5 eV/794.8 eV), Co-O (782.7 eV/796.4 eV), and Co-N_X (784.9 eV/798.3 eV)[18,32]. Notably, Co^0 is the major species at 49.9 % [Supplementary Table 2], indicating that Co species in Co SAs/NPs@N-CNTs mainly existed in the form of Co NPs, consistent with the TEM results. Furthermore, the Co 2p spectrum indicated the interaction between doped N atoms and Co, forming Co-N_X structures (accounting for 24.8% of Co-N_X), which caused the overall Co 2p spectrum of Co SAs/NPs@N-CNTs to shift toward lower binding energies compared to that of Co@CNTs. XPS analysis revealed Co contents of 0.3% for Co@CNTs and 0.5% for Co SAs/NPs@N-CNTs, corresponding to mass fractions of 1.3 wt% and 2.4 wt%, respectively. However, inductively coupled plasma mass spectrometry (ICP-MS) detected Co contents of 1.9 wt% for Co@CNTs and 1.4 wt% for Co SAs/NPs@N-CNTs. XPS can only measure the surface Co content of the samples; the actual Co content in the samples should refer to the value determined by ICP-MS. The samples were also subjected to H_2-temperature-programmed reduction (TPR) analysis [Supplementary Figure 4]. Notably, Co@CNTs exhibited distinct peaks at 355 and 428 °C, corresponding to the reduction of Co^{3+} and Co^{2+}, respectively[33,34]. In contrast, only a faint signal peak was observed at 359 °C for Co SAs/NPs@N-CNTs; the shift of peak positions towards higher temperature in Co SAs/NPs@N-CNTs suggested that Co species in Co SAs/NPs@N-CNTs were more difficult to reduce due to strong interactions between Co and N. The low intensity of the reduction peak was due to the Co species being predominantly present as Co NPs and Co-N_X in Co SAs/NPs@N-CNTs. Overall, these results indicated that besides existing in the form of Co NPs, Co species in Co SAs/NPs@N-CNTs also interacted with N to form Co-N_X structures, which might establish single atom active sites.

To further explore the coordination environment of Co species in Co SAs/NPs@N-CNTs, X-ray absorption near edge structure (XANES) spectra at the Co K-edge were conducted. According to Figure 4A, the absorption edge of Co SAs/NPs@N-CNTs fell between that of Co foil and CoO, indicating that the valence

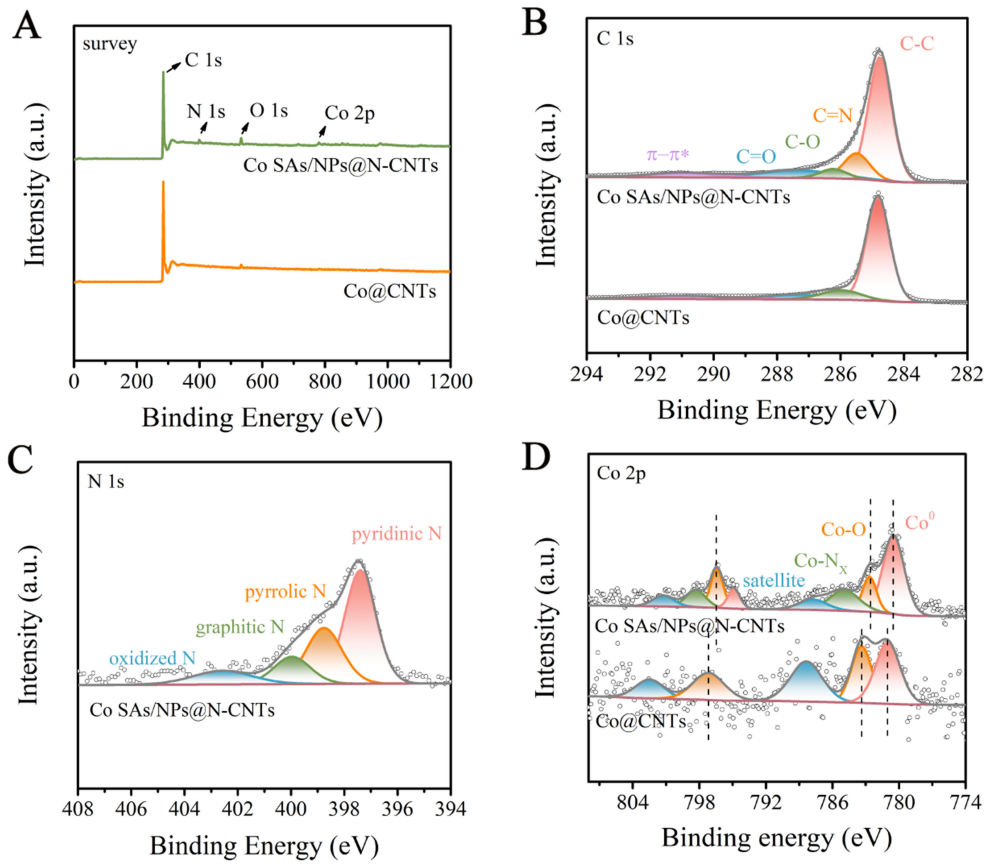

Figure 3. (A) XPS full spectra; high-resolution XPS spectra for (B) C 1s, (C) N 1s and (D) Co 2p of Co@CNTs and Co SAs/NPs@N-CNTs. XPS: X-ray photoelectron spectroscopy; CNTs: carbon nanotubes; SAs: single atoms; NPs: nanoparticles.

state of Co ranged from 0 to +2. Figure 4B presented the Fourier transform extended X-ray absorption fine structure (FT-EXAFS) spectra in R space, revealing distinct peaks at 1.52 Å and 2.12 Å, corresponding to Co-N and Co-Co coordination, respectively[21,35]. Based on the EXAFS data in R space, the average coordination numbers of Co species in Co SAs/NPs@N-CNTs were determined, revealing a Co-N coordination number of 2.4 and a Co-Co coordination number of 4.6 [Figure 4C and Supplementary Table 3]. And wavelet transform (WT) plots also exhibited signals attributed to Co-N and Co-Co coordination at 5.83 $Å^{-1}$ and 8.00 $Å^{-1}$, respectively, consistent with the above result [Figure 4D-F]. Above analysis further confirmed that Co species predominantly exist as Co SAs and Co NPs in Co SAs/NPs@N-CNTs.

Catalytic performance test

According to previous studies, the selective oxidation of HMF to FDCA involves a complex tandem reaction with two main pathways: (1) HMF → HMFCA → FFCA → FDCA, and (2) HMF → DFF → FFCA → FDCA. The intermediate products in both pathways are indeed present and exhibit certain stability. To achieve high yield towards the final product FDCA, it is crucial to facilitate the complete conversion of HMF into various intermediates and promote subsequent transformation of intermediates into FDCA. Without a catalyst, the oxidation of HMF by TBHP can achieve a conversion of 94.2% [Figure 5A and Supplementary Table 4]. However, the reaction mainly stalled at the intermediate stages, and only about 13.7% of HMF transformed into FDCA, with approximately 20% of the HMF converting into other byproducts. CNTs exhibited catalytic activity almost equivalent to the without catalyst system. When Co SAs/NPs@N-CNTs were employed, the production of byproducts significantly decreased, resulting in a

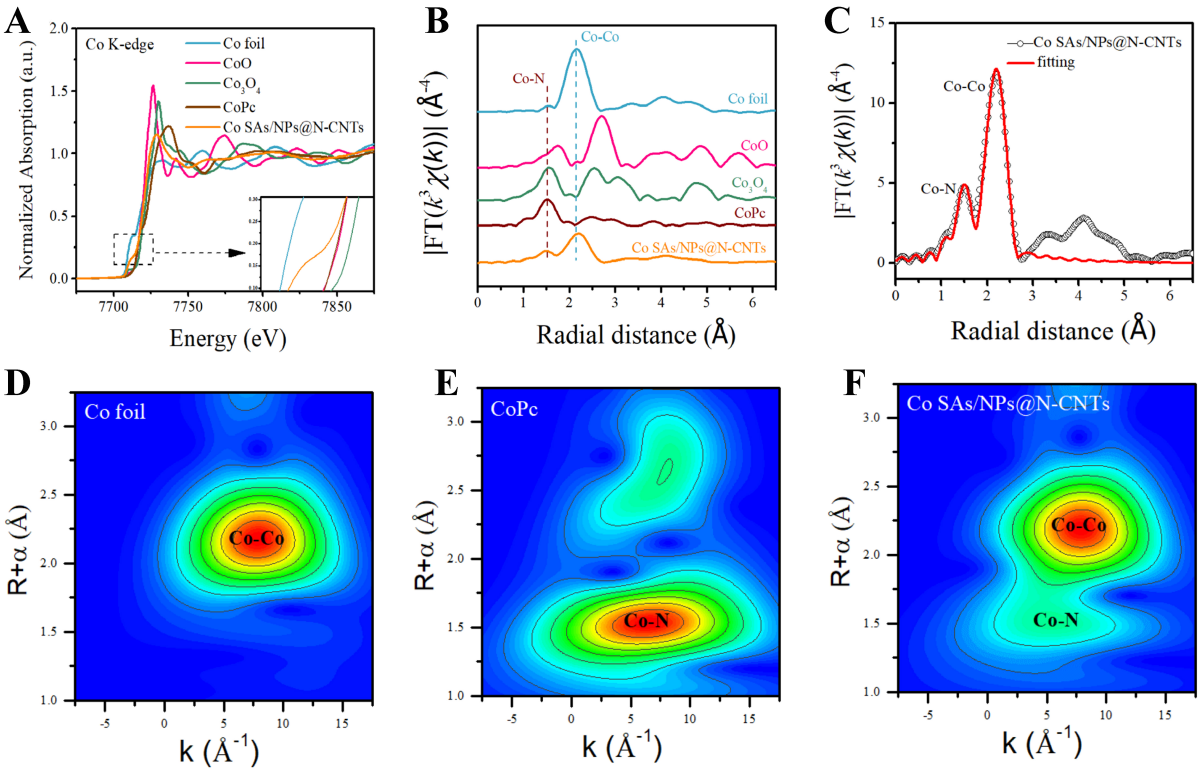

Figure 4. (A) XANES spectra and (B) FT-EXAFS spectra of Co SAs/NPs@N-CNTs, Co foil, CoO, Co_3O_4 and CoPc at Co K-edge; (C) FT-EXAFS fitting curve of Co SAs/NPs@N-CNTs in R space; Wavelet transform K^3-weighted EXAFS plots of (D) Co foil, (E) CoPc and (F) Co SAs/NPs@N-CNTs. XANES: X-ray absorption near edge structure; FT-EXAFS: Fourier transform extended X-ray absorption fine structure; SAs: single atoms; NPs: nanoparticles; CNTs: carbon nanotubes.

total HMF conversion of 98.6%, with 94.2% of HMF being converted into FDCA. This indicated that Co SAs/NPs@N-CNTs can efficiently convert HMF into various intermediates and promote their highly selective transformation into FDCA. In contrast, Co@CNTs only exhibited weak catalytic activity, comparable to the system without a catalyst. Earlier characterization results suggested that Co species in Co@CNTs primarily existed as CoO_X nanoparticles, while in Co SAs/NPs@N-CNTs, Co species existed in the form of Co SAs and Co NPs. Moreover, the Co content in Co@CNTs is higher than that in Co SAs/NPs@N-CNTs (Co contents of 1.9 wt% for Co@CNTs and 1.4 wt% for Co SAs/NPs@N-CNTs). Combining above statements with the results of catalytic activity test, it becomes evident that CoO_X nanoparticles cannot efficiently convert HMF to FDCA, whereas the coexistence of Co SAs and Co NPs system can do it in the reaction condition. The conclusion is consistent with the result of intrinsic kinetic experiments [Figure 5B-D]. When considering HMF, DFF, and FFCA as reactants, the oxidation processes of these three compounds over Co SAs/NPs@N-CNTs all exhibited lower apparent activation energy than that of Co@CNTs. This indicated that Co SAs/NPs@N-CNTs exhibited significantly faster kinetics than Co@CNTs, explaining the superior catalytic performance of Co SAs/NPs@N-CNTs.

To distinguish the contributions of Co SAs and Co NPs in Co SAs/NPs@N-CNTs to the selective oxidation of HMF, three control experiments were conducted: (1) Co SAs/NPs@N-CNTs were further acid-treated to remove Co NPs, labeled as Co SAs@N-CNTs (Co SAs only), Co SAs@N-CNTs were employed for the oxidation of HMF. The acid treatment procedure is described in Section "Synthesis of Co SAs/NPs@N-CNTs and Co SAs@N-CNTs"; (2) In the oxidation of HMF on Co SAs/NPs@N-CNTs, additional potassium thiocyanate (KSCN) was introduced to poison the Co SAs, labeled as Co NPs@N-CNTs (Co NPs

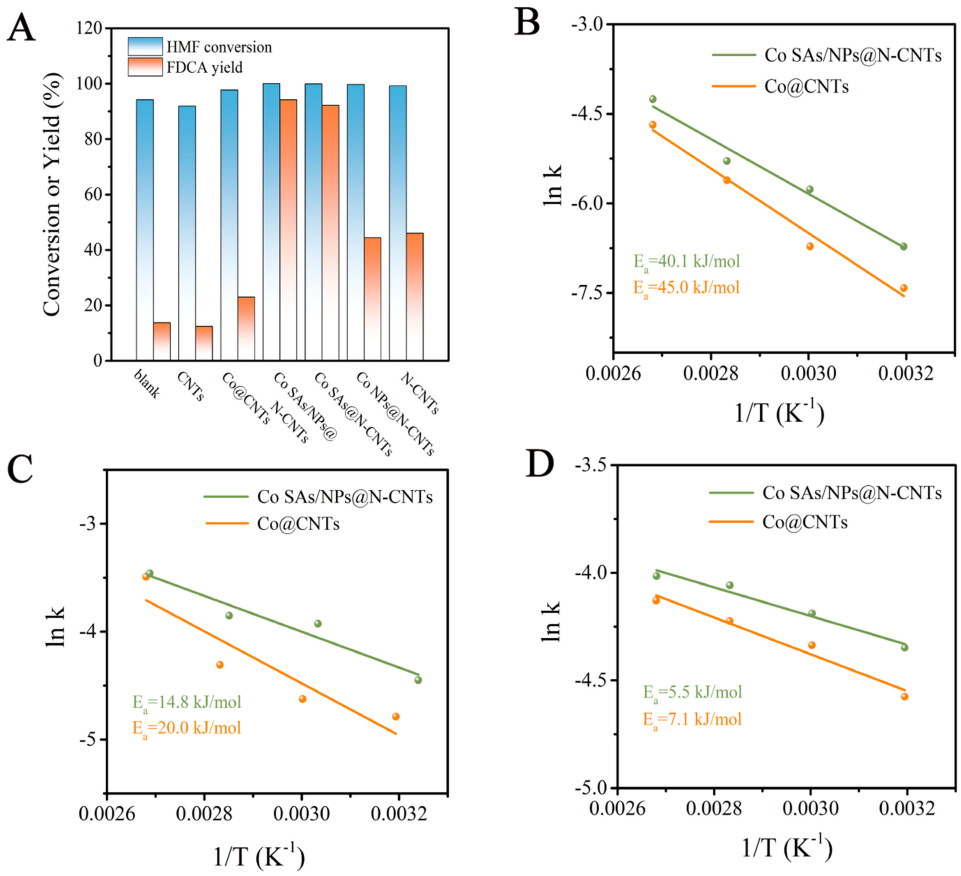

Figure 5. (A) The selective oxidation of HMF on different catalysts. Kinetic experiments of the oxidation of (B) HMF, (C) DFF and (D) FFCA over Co@CNTs and Co SAs/NPs@N-CNTs. HMF: 5-hydroxymethylfurfural; DFF: 2,5-diformylfuran; FFCA: 5-formyl-2-furancarboxylic acid; CNTs: carbon nanotubes; SAs: single atoms; NPs: nanoparticles.

only); (3) Co SAs@N-CNTs were used for the oxidation of HMF, and additional KSCN was added to poison the Co SAs, labeled as N-CNTs (nitrogen-doped carbon-based substrate only). As shown in Supplementary Table 4, after 24 h of reaction, Co SAs@N-CNTs still achieved a FDCA yield of 92.2%, while Co NPs@N-CNTs and N-CNTs all only reached about 45% FDCA yield and most of the products remained in the stage of FFCA intermediate. These results indicated that in this reaction system, Co SAs are the primary active sites, efficiently converting HMF to the final product FDCA. To gain a more intuitive understanding of the impact of each catalyst on the process of selective oxidation of HMF, time-conversion/yield curves were obtained. According to Figure 6, in this system, the oxidation of HMF to FDCA tends to follow pathway (2), where HMF was transformed to DFF and then to FDCA. No matter which catalyst was used, the transformation of HMF to HMFCA/DFF intermediates was relatively rapid, with over 90% conversion achieved in 6 h. However, at this point, the FDCA yield for Co SAs@N-CNTs, Co NPs@N-CNTs and N-CNTs was all below 20%, while Co SAs/NPs@N-CNTs surprisingly reached 36.2% FDCA yield, demonstrating a faster reaction rate than other catalysts [Figure 6A and B]. After 12 h of reaction, Co SAs/NPs@N-CNTs achieved an FDCA yield of 81.4%, whereas Co SAs@N-CNTs only exhibited 57% yield for FDCA. It was not until 24 h later that the reaction reached equilibrium, causing the catalytic effects of Co SAs/NPs@N-CNTs and Co SAs@N-CNTs to be nearly identical. These results indicated that in the early stage of the reaction, Co SAs/NPs@N-CNTs exhibited a more rapid rate for the oxidation of HMF to FDCA than Co SAs@N-CNTs, implying that Co NPs in Co SAs/NPs@N-CNTs significantly contribute to enhancing the reaction. Figure 6C and D illustrated that Co NPs@N-CNTs and N-CNTs exhibited

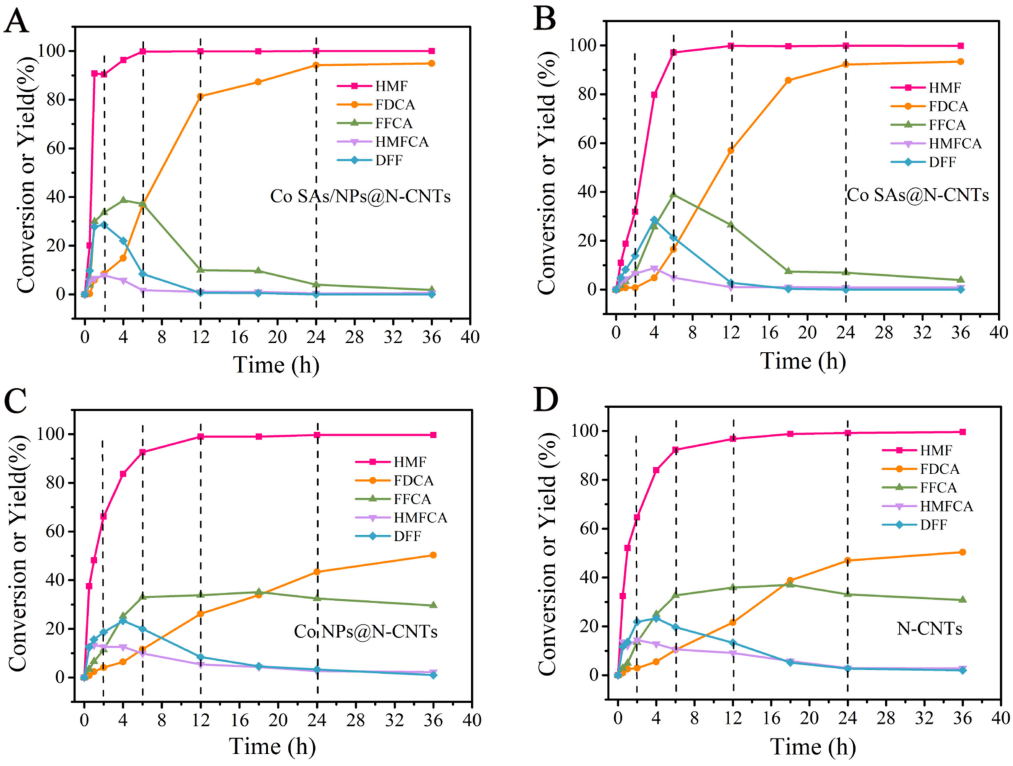

Figure 6. Conversion of HMF and yield of products over (A) Co SAs/NPs@N-CNTs, (B) Co SAs@N-CNTs, (C) Co NPs@N-CNTs and (D) N-CNTs in different reaction times. HMF: 5-hydroxymethylfurfural; SAs: single atoms; NPs: nanoparticles; CNTs: carbon nanotubes.

comparable reaction processes for the conversion of HMF and the subsequent transformation of intermediates to FDCA, suggesting that aside from the role of Co SAs in Co SAs/NPs@N-CNTs, the remaining Co NPs displayed minimal activity in the selective oxidation of HMF. Co NPs@N-CNTs just displayed the catalytic activity of the nitrogen-doped carbon substrate, indicating that Co NPs in Co SAs/NPs@N-CNTs did not act as active sites in the reaction. To sum up, Co SAs were the primary active sites in Co SAs/NPs@N-CNTs, and the Co NPs coexisting did not directly participate as active sites in the oxidation of HMF. Instead, Co NPs assisted the Co SAs active sites in facilitating the conversion of HMF and subsequent transformation of intermediates towards FDCA. Additionally, the turnover frequency (TOF) value of Co SAs/NPs@N-CNTs for the oxidation of HMF to prepare FDCA was calculated according to the experimental results. The TOF value is even comparable to that of several reported metal-based catalysts [Table 1].

From the time-conversion/yield curves, it was evident that achieving complete conversion of HMF was relatively rapid. The rate-limiting step in the oxidation of HMF to FDCA lies in the further conversion of intermediates. Thus, using DFF and FFCA as substrates, respectively, Co SAs/NPs@N-CNTs and Co SAs@N-CNTs as catalysts, time-conversion/yield curves were generated to calculate the respective reaction rate constants [Supplementary Table 5]. Experimental results indicated that the reaction rate constants for both DFF and FFCA conversions were higher with Co SAs/NPs@N-CNTs compared to those with Co SAs@N-CNTs as the catalyst (k_{DFF}: 0.02109 min^{-1} > 0.01348 min^{-1}, k_{FFCA}: 0.01727 min^{-1} > 0.01174 min^{-1}). This suggested that Co SAs/NPs@N-CNTs were more conducive to the conversion of DFF and FFCA intermediates than Co SAs/@N-CNTs. Furthermore, the rate constant for the further conversion of FFCA intermediates is significantly lower than that for DFF intermediates, demonstrating that the conversion of

Table 1. Comparison of TOF values of Co SAs/NPs@N-CNTs with other catalysts

Sample	TOF_{HMF} (s^{-1})	TOF_{FDCA} (s^{-1})	Ref.
Co SAs/NPs@N-CNTs	0.19	0.062	This work
Pd-MnO_2	-	0.042	[12]
Ru_1/NiO	0.016	-	[36]
FeN_X/C-900	0.0019	-	[37]
$Co_{1.4}$-Cu-CN_X	0.057	-	[38]
Ru-Mn-2	-	0.0061	[39]
CoO-$CoSe_2$	-	0.046	[40]
Pt/3D-$Ce_{0.8}La_{0.2}O_{2-\delta}$	-	0.067	[41]
Au-Cu/γ-Al_2O_3	0.0675	-	[42]
CuO/m-Al_2O_3	0.00016	-	[43]
Au/CeO_2-cube	-	0.015	[44]
Pt@rGO/$Sn_{0.8}$	0.185	-	[45]

TOF: Turnover frequency; SAs: single atoms; NPs: nanoparticles; CNTs: carbon nanotubes.

FFCA is the rate-determining step in the oxidation of HMF to FDCA.

Mechanism of HMF oxidation

The addition of BHT, a radical scavenger, into the reaction system caused a notable reduction in the catalytic activity of Co SAs/NPs@N-CNTs, with an FDCA yield of only 2.0%. This indicated that in this reaction system, the oxidation of HMF to FDCA is a radical-based process. Based on relevant literature[46,47], the following possible reaction mechanism was proposed [Figure 7]: firstly, TBHP (BuOOH) dissociated into BuO· and ·OH under the action of Co SAs/NPs@N-CNTs. The oxygen atom on the -OH group of the HMF molecule adsorbed onto the active sites of Co SAs, removing the H from the -OH group to form intermediate **a**. BuO· removed the H from the -CH_2- group on intermediate **a**, yielding DFF and BuOH. Subsequently, DFF underwent nucleophilic addition with H_2O to form an aldehyde intermediate **b**. The oxygen atom on the -OH group of intermediate **b** adsorbed again onto the active sites of Co SAs, removing the H from the -OH group to form intermediate **c**. BuO· abstracted the H from -CH- in intermediate **c**, resulting in the formation of FFCA and BuOH. The -CHO group in FFCA underwent nucleophilic addition with H_2O and dehydrogenation processes, leading to the formation of -COOH, thus yielding FDCA. According to the previous analysis results, during the reaction process, Co SAs served as the adsorption active sites for the reaction, while adjacent Co NPs assisted Co SAs in facilitating the conversion of HMF into various intermediates and further transformation of intermediates into FDCA.

Recycle experiment

Furthermore, the recyclability of Co SAs/NPs@N-CNTs in the oxidation of HMF was assessed, with the test results provided in Supplementary Table 6. Co SAs/NPs@N-CNTs maintained a HMF conversion of 96.0% after three cycles (Co SAs/NPs@N-CNTs after three repeated experiments denoted as Co SAs/NPs@N-CNTs-R_3), but the FDCA yield dropped to 22.8%. N_2 adsorption-desorption measurement for Co SAs/NPs@N-CNTs-R_3 [Supplementary Figure 3 and Supplementary Table 1] indicated that the pore structure did not undergo significant changes after three cycles. Co SAs/NPs@N-CNTs-R_3 were also subjected to 600 °C calcination in nitrogen atmosphere, resulting in Co SAs/NPs@N-CNTs-R_3-600 °C with an FDCA yield of only 29.4%. This suggested that the deactivation of catalyst is not due to pore blockage or the residual products. ICP-MS analysis revealed that the Co content in Co SAs/NPs@N-CNTs decreased from 1.40 wt% to 0.47 wt% after three cycles, indicating a significant loss of Co species during the recycling process. Combining this with the ICP-MS result of Co SAs@N-CNTs (Co content of 0.95 wt%), it can be inferred that the loss of Co species included not only unstable Co NPs but also a portion of Co SAs sites.

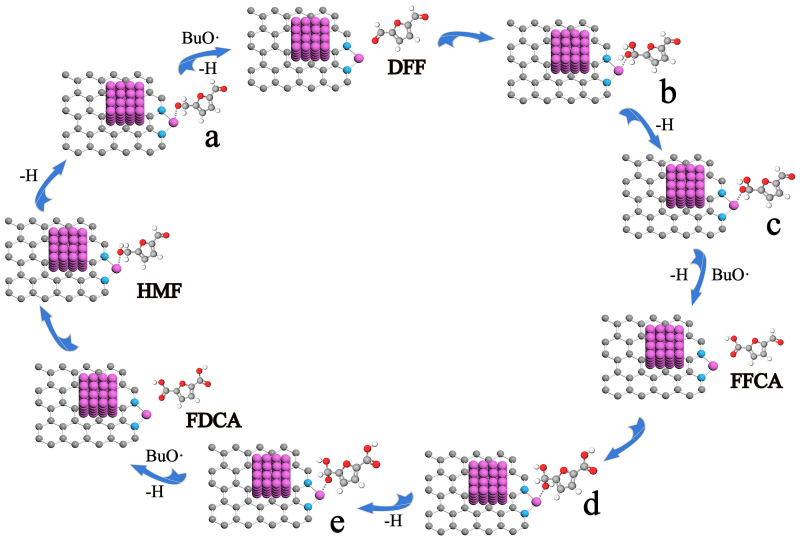

Figure 7. The possible reaction mechanism for the oxidation of HMF to FDCA on Co SAs/NPs@N-CNTs. HMF: 5-hydroxymethylfurfural; FDCA: 2,5-furandicarboxylic acid; SAs: single atoms; NPs: nanoparticles; CNTs: carbon nanotubes.

XPS analysis of Co SAs/NPs@N-CNTs-R_3 also showed a decrease in N content from 3.3% to 2.4%, aligning with the loss of Co SAs sites [Supplementary Figure 5 and Supplementary Table 2]. TEM images of Co SAs/NPs@N-CNTs-R_3 [Supplementary Figure 6] revealed that the morphology of CNTs remained intact, but a noticeable reduction in Co NPs was observed. The aforementioned analyses collectively indicated that both Co species and N elements are lost in Co SAs/NPs@N-CNTs after three cycles, resulting in a substantial reduction in catalytic performance on account of the diminished presence of Co NPs and Co SAs active sites.

CONCLUSIONS

In summary, a catalyst featuring the coexistence of Co SAs and Co NPs was constructed on CNTs through a simple method. Due to the synergistic effect between Co SAs and Co NPs, this catalyst exhibited excellent catalytic activity in the selective oxidation of HMF to FDCA, achieving 100% HMF conversion and 94.2% FDCA yield. During the reaction, HMF molecules adsorbed onto the active sites of Co SAs active sites, while Co NPs did not directly serve as active sites but instead assisted the Co SAs active sites to efficiently convert HMF into DFF and FFCA intermediates and promoted the further transformation of DFF and FFCA intermediates into FDCA. Moreover, the catalytic performance of the catalyst is even comparable to that of several reported metal-based catalysts.

DECLARATIONS

Authors' contributions

Made substantial contributions to conception and design of the study and performed data analysis and interpretation: Yi C

Provided administrative, technical, and material support: Liu Z

Availability of data and materials

The detailed characterizations and methods are available in the Supplementary Materials. Other raw data that support the findings of this study are available from the corresponding author upon reasonable request.

Financial support and sponsorship

This work was financially supported by the National Natural Science Foundation of China (No. 22372056), the Science and Technology Innovation Program of Hunan Province (Grant 2022SK2064) and the State Key Laboratory of Heavy Oil Processing, China University of Petroleum.

Conflicts of interest

Both authors declared that there are no conflicts of interest.

Ethical approval and consent to participate

Not applicable.

Consent for publication

Not applicable.

REFERENCES

1. Zia KM, Noreen A, Zuber M, Tabasum S, Mujahid M. Recent developments and future prospects on bio-based polyesters derived from renewable resources: a review. *Int J Biol Macromol* 2016;82:1028-40. DOI PubMed
2. Ilkaeva M, Krivtsov I, García-López EI, et al. Selective photocatalytic oxidation of 5-hydroxymethylfurfural to 2,5-furandicarboxaldehyde by polymeric carbon nitride-hydrogen peroxide adduct. *J Catal* 2018;359:212-22. DOI
3. Kanetaka Y, Yamazaki S, Kimura K. Preparation of poly(ether ketone)s derived from 2,5-furandicarboxylic acid by polymerization in ionic liquid. *Macromolecules* 2016;49:1252-8. DOI
4. Payne J, Jones MD. The chemical recycling of polyesters for a circular plastics economy: challenges and emerging opportunities. *ChemSusChem* 2021;14:4041-70. DOI PubMed PMC
5. Parida D, Aerts A, Vanbroekhoven K, et al. Monomer recycling of polyethylene terephthalate, polycarbonate and polyethers: scalable processes to achieve high carbon circularity. *Prog Polym Sci* 2024;149:101783. DOI
6. Chen G, van Straalen NM, Roelofs D. The ecotoxicogenomic assessment of soil toxicity associated with the production chain of 2,5-furandicarboxylic acid (FDCA), a candidate bio-based green chemical building block. *Green Chem* 2016;18:4420-31. DOI
7. Eerhart AJJE, Faaij APC, Patel MK. Replacing fossil based PET with biobased PEF; process analysis, energy and GHG balance. *Energy Environ Sci* 2012;5:6407. DOI
8. Trapasso G, Annatelli M, Dalla Torre D, Aricò F. Synthesis of 2,5-furandicarboxylic acid dimethyl ester from galactaric acid *via* dimethyl carbonate chemistry. *Green Chem* 2022;24:2766-71. DOI
9. Zhao D, Delbecq F, Len C. One-pot FDCA diester synthesis from mucic acid and their solvent-free regioselective polytransesterification for production of glycerol-based furanic polyesters. *Molecules* 2019;24:1030. DOI PubMed PMC
10. Liao YT, Nguyen VC, Ishiguro N, Young AP, Tsung CK, Wu KCW. Engineering a homogeneous alloy-oxide interface derived from metal-organic frameworks for selective oxidation of 5-hydroxymethylfurfural to 2,5-furandicarboxylic acid. *Appl Catal B Environ* 2020;270:118805. DOI
11. Bonincontro D, Lolli A, Villa A, et al. AuPd-nNiO as an effective catalyst for the base-free oxidation of HMF under mild reaction conditions. *Green Chem* 2019;21:4090-9. DOI
12. Liao X, Hou J, Wang Y, et al. An active, selective, and stable manganese oxide-supported atomic Pd catalyst for aerobic oxidation of 5-hydroxymethylfurfural. *Green Chem* 2019;21:4194-203. DOI
13. Liguori F, Barbaro P, Calisi N. Continuous-flow oxidation of HMF to FDCA by resin-supported platinum catalysts in neat water. *ChemSusChem* 2019;12:2558-63. DOI PubMed
14. Yang C, Li X, Zhang Z, et al. High efficient catalytic oxidation of 5-hydroxymethylfurfural into 2,5-furandicarboxylic acid under benign conditions with nitrogen-doped graphene encapsulated Cu nanoparticles. *J Energy Chem* 2020;50:96-105. DOI
15. Zhang S, Sun X, Zheng Z, Zhang L. Nanoscale center-hollowed hexagon $MnCo_2O_4$ spinel catalyzed aerobic oxidation of 5-hydroxymethylfurfural to 2,5-furandicarboxylic acid. *Catal Commun* 2018;113:19-22. DOI
16. Su T, Zhao D, Wang Y, Lü H, Varma RS, Len C. Innovative protocols in the catalytic oxidation of 5-hydroxymethylfurfural. *ChemSusChem* 2021;14:266-80. DOI PubMed
17. Dai K, Zhang N, Zhang L, Yin L, Zhao Y, Zhang B. Self-supported Co/CoO anchored on N-doped carbon composite as bifunctional electrocatalyst for efficient overall water splitting. *Chem Eng J* 2021;414:128804. DOI
18. Yi C, Huo J, Liu Z. Co single atoms and CoO clusters over nitrogen-doped hollow carbon spheres for synergistic oxidation of aromatic alkanes. *Chem Eng J* 2023;467:143541. DOI

19. Tan Y, Zhu W, Zhang Z, et al. Electronic tuning of confined sub-nanometer cobalt oxide clusters boosting oxygen catalysis and rechargeable Zn-air batteries. *Nano Energy* 2021;83:105813. DOI
20. Xiang G, Zhang L, Chen J, Zhang B, Liu Z. A binary carbon@silica@carbon hydrophobic nanoreactor for highly efficient selective oxidation of aromatic alkanes. *Nanoscale* 2021;13:18140-7. DOI PubMed
21. Wang M, Li M, Zhao Y, et al. Construction of N-doped carbon frames anchored with Co single atoms and Co nanoparticles as robust electrocatalyst for hydrogen evolution in the entire pH range. *J Energy Chem* 2022;67:147-56. DOI
22. Sa YJ, Park SO, Jung GY, et al. Heterogeneous Co-N/C electrocatalysts with controlled cobalt site densities for the hydrogen evolution reaction: structure-activity correlations and kinetic insights. *ACS Catal* 2019;9:83-97. DOI
23. Yi C, Zhang L, Xiang G, Liu Z. Size effect of Co-N-C-functionalized mesoporous silica hollow nanoreactors on the catalytic performance for the selective oxidation of ethylbenzene. *New J Chem* 2022;46:15102-9. DOI
24. Yi C, Zhang L, Xiang G, Chen X, Cheng N, Liu Z. N-rich porous carbon catalysts with huge surface areas from bean curd activated by K_2CO_3. *New J Chem* 2021;45:16469-76. DOI
25. Bi F, Feng X, Zhou Z, et al. Mn-based catalysts derived from the non-thermal treatment of Mn-MIL-100 to enhance its water-resistance for toluene oxidation: Mechanism study. *Chem Eng J* 2024;485:149776. DOI
26. Bi F, Wei J, Gao B, et al. New insight into the antagonism mechanism between binary VOCs during their degradation over Pd/ZrO_2 catalysts. *ACS EST Eng* 2024;4:1346-55. DOI
27. Chen C, Wang ZQ, Gong YY, et al. Cobalt embedded in nitrogen-doped porous carbon as a robust heterogeneous catalyst for the atom-economic alcohol dehydrogenation to carboxylic acids. *Carbon* 2021;174:284-94. DOI
28. Chen X, Cheng XB, Liu Z. High sulfur-doped hard carbon anode from polystyrene with enhanced capacity and stability for potassium-ion storage. *J Energy Chem* 2022;68:688-98. DOI
29. Xiang G, Zhang L, Yi C, Liu Z. One-pot pyrolysis method to fabricate Co/N co-doped hollow mesoporous spheres with carbon/silica binary shells for selective oxidation of arylalkanes. *Appl Surf Sci* 2022;577:151829. DOI
30. Zhang L, Jie S, Cheng N, Liu Z. Solvent-free melting-assisted pyrolysis strategy applied on the Co/N codoped porous carbon catalyst. *ACS Sustainable Chem Eng* 2019;7:19474-82. DOI
31. Zhang L, Jie S, Liu Z. Bicontinuous mesoporous Co, N co-doped carbon catalysts with high catalytic performance for ethylbenzene oxidation. *New J Chem* 2019;43:7275-81. DOI
32. Son HJ, Kim MJ, Ahn SH. Monolithic Co-N-C membrane integrating Co atoms and clusters as a self-supporting multi-functional electrode for solid-state zinc-air batteries and self-powered water splitting. *Chem Eng J* 2021;414:128739. DOI
33. Yang Q, Choi H, Al-Abed SR, Dionysiou DD. Iron-cobalt mixed oxide nanocatalysts: heterogeneous peroxymonosulfate activation, cobalt leaching, and ferromagnetic properties for environmental applications. *Appl Catal B Environ* 2009;88:462-9. DOI
34. Liu S, Wang H, Wang S, et al. Engineering morphology and Ni substitution of $Ni_xCo_{3-x}O_4$ spinel oxides to promote catalytic combustion of ethane: elucidating the influence of oxygen defects. *ACS Catal* 2023;13:4683-99. DOI
35. Zhang X, Xu X, Yao S, et al. Boosting electrocatalytic activity of single atom catalysts supported on nitrogen-doped carbon through N coordination environment engineering. *Small* 2022;18:e2105329. DOI
36. Liu Y, Gan T, He Q, Zhang H, He X, Ji H. Catalytic oxidation of 5-hydroxymethylfurfural to 2,5-diformylfuran over atomically dispersed ruthenium catalysts. *Ind Eng Chem Res* 2020;59:4333-7. DOI
37. Ke Q, Jin Y, Ruan F, et al. Boosting the activity of catalytic oxidation of 5-hydroxymethylfurfural to 2,5-diformylfuran over nitrogen-doped manganese oxide catalysts. *Green Chem* 2019;21:4313-8. DOI
38. Jing T, Yang S, Feng Y, Li T, Zuo Y, Rao D. Selective and effective oxidation of 5-hydroxymethylfurfural by tuning the intermediates adsorption on Co-Cu-CN_x. *Nano Res* 2023;16:6670-8. DOI
39. Pal P, Saravanamurugan S. Enhanced basicity of MnOx-supported Ru for the selective oxidation of 5-hydroxymethylfurfural to 2,5-furandicarboxylic acid. *ChemSusChem* 2022;15:e202200902. DOI PubMed
40. Huang X, Song J, Hua M, et al. Enhancing the electrocatalytic activity of CoO for the oxidation of 5-hydroxymethylfurfural by introducing oxygen vacancies. *Green Chem* 2020;22:843-9. DOI
41. Yang W, Yu H, Wang B, et al. Leveraging Pt/$Ce_{1-x}La_xO_{2-\delta}$ to elucidate interfacial oxygen vacancy active sites for aerobic oxidation of 5-hydroxymethylfurfural. *ACS Appl Mater Interfaces* 2022;14:37667-80. DOI PubMed
42. Du J, Fang H, Qu H, Zhang J, Duan X, Yuan Y. Fabrication of supported Au-CuO_x nanohybrids by reduction-oxidation strategy for efficient oxidative esterification of 5-hydroxymethyl-2-furfural into dimethyl furan-2,5-dicarboxylate. *Appl Catal A General* 2018;567:80-9. DOI
43. Gupta SSR, Vinu A, Kantam ML. Copper-catalyzed oxidative methyl-esterification of 5-hydroxymethylfurfural using TBHP as an oxidizing and methylating reagent: a new approach for the synthesis of furan-2,5-dimethylcarboxylate. *J Catal* 2020;389:259-69. DOI
44. Li Q, Wang H, Tian Z, et al. Selective oxidation of 5-hydroxymethylfurfural to 2,5-furandicarboxylic acid over Au/CeO_2 catalysts: the morphology effect of CeO_2. *Catal Sci Technol* 2019;9:1570-80. DOI
45. García-Zaragoza A, Cerezo-Navarrete C, Oña-Burgos P, Martínez-Prieto LM. Boosting the catalytic performance of graphene-supported Pt nanoparticles via decorating with -$SnBu_n$: an efficient approach for aqueous hydrogenation of biomass-derived compounds. *Nanoscale* 2023;15:12319-32. DOI PubMed
46. Cheng F, Guo D, Lai J, et al. Efficient base-free oxidation of 5-hydroxymethylfurfural to 2,5-furandicarboxylic acid over copper-doped manganese oxide nanorods with *tert*-butanol as solvent. *Front Chem Sci Eng* 2021;15:960-8. DOI
47. Gao D, Han F, Waterhouse GI, Li Y, Zhang L. NiFe layered double hydroxide-derived catalysts with remarkable selectivity for the oxidation of 5-hydroxymethylfurfural to 2,5-furanedicarboxylic acid under base-free conditions. *ACS Sustainable Chem Eng* 2023;11:1557-68. DOI